Experimentally derived luminous efficiencies for aluminum and iron at meteoric speeds

L. K. Tarnecki[1], R. A. Marshall[1], J. Fontanese[2,3], Z. Sternovsky[2,1], T. Munsat[3,4]

[1]Aerospace Engineering Sciences, University of Colorado Boulder, 3775 Discovery Drive Boulder, CO 80303
[2]Laboratory for Atmospheric and Space Physics, University of Colorado Boulder, 1234 Innovation Dr Boulder, CO 80303
[3]Institute for Modeling Plasmas, Atmospheres, and Cosmic Dust, University of Colorado Boulder, 3400 Marine Street Boulder, CO 80304
[4]Department of Physics, University of Colorado, 390 UCB, Boulder, CO 80309

Key Points:

- Laboratory ablation experiments were performed to characterize luminous efficiencies for iron and aluminum at velocities greater than 10 km/s
- Empirical curve fits are derived to relate the luminous efficiency and particle velocity for both species
- Differences in iron and aluminum results indicate that the luminous efficiency varies with composition

Corresponding author: Liane Tarnecki, `liane.tarnecki@colorado.edu`

Abstract

Calculating meteoroid masses from photometric observations relies on prior knowledge of the luminous efficiency, a parameter that is not well characterized; reported values vary by several orders of magnitude. We present results from an experimental campaign to determine the luminous efficiency as a function of mass, velocity, and composition. Using a linear electrostatic dust accelerator, iron and aluminum microparticles were accelerated to 10+ km/s and ablated, and the light production measured. The luminous efficiency of each event was calculated and functional forms fit for each species. For both materials, the luminous efficiency is lowest at low velocities, rises sharply, then falls as velocity increases. However, the exact shape and magnitude of the curve is not consistent between the materials. The difference between the luminous efficiencies for iron and aluminum, particularly at high velocities, indicates that it is not sufficient to use the same luminous efficiency for all compositions and velocities.

Plain Language Summary

Material left behind by meteoroids and interplanetary dust particles entering Earth's atmosphere are important drivers of atmospheric phenomena and chemistry. There is large spread in estimates of the total meteoric mass input, in part due to uncertainty in several key parameters that are required to make mass estimates of individual particles. This work presents an experimental campaign to characterize one such parameter, the luminous efficiency, in a laboratory setting. The luminous efficiency describes the amount of a meteoroid's kinetic energy that is converted into light energy; large uncertainty in historical measurements of the luminous efficiency directly correspond to large uncertainties in mass estimates made from optical observations. The results show that there is significant variation in the luminous efficiency as a function of both particle velocity and composition, indicating that relying on a single value for the luminous efficiency is not sufficient in all cases.

1 Introduction

Meteoroids and interplanetary dust are the main sources of metal input into the atmosphere. The amount of injected meteoric material has significant consequences for the atmosphere both in terms of composition, chemistry and the formation of metal layers and noctilucent clouds, and for our understanding of vertical transport and the distribution of dust in the solar system (Plane, 2012). However, there is wide variation in estimates of the total mass input from meteoroids and dust depending on the measurement technique. Even studies using the same technique can produce large variation in the resulting estimate, due to differences in assumptions and analysis process (e.g. Mathews et al., 2001; Dyrud et al., 2004; Bland et al., 1996).

Optical cameras provide a relatively cheap and easily deployed method for meteor observation. Many all-sky camera networks have been developed to detect meteors over relatively large regions (e.g., Brown et al., 2010; Vida et al., 2021; Spurný & Borovička, 2002). By employing multiple cameras, it is possible to determine the location and velocity of the meteoroid and to measure the light output. In general, optical observations are made in a limited spectral band; in order to consider the total energy emitted, one must convert between the brightness in the measured band and the absolute luminosity (Ceplecha et al., 1998). This conversion is complicated by the lack of composition information available for the vast majority of observed meteors.

Photometric masses are calculated by relating luminosity (L) to the change in the meteoroid's kinetic energy (E_k) (Equation 1). The parameter relating the two is called the luminous efficiency (τ), which describes the fraction of the kinetic energy that is converted into light energy. As both the particle mass (m) and deceleration (dv/dt) are as-

sumed to be relatively small, the second term in Equation 1 is frequently considered to be small compared to the first term and has historically been neglected (e.g. Ceplecha (1966); Campbell-Brown et al. (2012)). Of the remaining terms, the luminosity and velocity are readily measurable by optical cameras.

$$\begin{aligned} L &= -\tau \left(\frac{dE_k}{dt} \right) \\ &= -\tau \left(\frac{1}{2} v^2 \frac{dm}{dt} + mv \frac{dv}{dt} \right) \end{aligned} \tag{1}$$

Since the mass and the luminous efficiency cannot be simultaneously measured by a single observation, photometric mass estimates depend on accurate prior knowledge of τ. However, estimates of the luminous efficiency, determined through observation, experiment, or theoretical analysis, are subject to large variation (Subasinghe & Campbell-Brown, 2018). The dependence of τ on velocity, composition, ablation altitude, particle mass, or any number of other parameters is not well known. In the absence of a consensus on the functional form of τ, a constant value, usually on the order of 1%, is sometimes used (Campbell-Brown, M. D. & Koschny, D., 2004).

This work will focus on an experimental method for determining τ in the laboratory. Laboratory experiments investigating the luminous efficiency of meteors were first performed in the 1970s (Becker & Friichtenicht, 1971; Becker & Slattery, 1973). These experiments simulated ablation by accelerating microparticles into pressurized chambers and observing the resulting light output. However, hardware constraints restricted the apparatus to a single-channel detector and limited the number of observed particles. The authors note that due to these limitations their goal was to observe possible trends rather than to measure τ precisely; therefore these studies reported only averaged results without error quantification and did not determine a functional form.

Further experiments using dust accelerators to investigate τ have not been performed since. This work presents an updated optical apparatus to be used with a dust accelerator to simulate ablation in the laboratory (Section 2). Iron and aluminum particles were accelerated to meteoric speeds and ablated, and the emitted optical signals recorded (Section 3). The resulting estimates and functional forms for τ for each species are reported (Section 4) and discussed in the context of previous work (Section 5).

2 Methodology

This experimental campaign was conducted at the University of Colorado's IMPACT laboratory, utilizing a 3 MV linear electrostatic dust accelerator, which accelerates micron and sub-micron charged dust grains to velocities ranging from 0.3 to 120 km/s (Shu et al., 2012). Accelerated particles pass uninterrupted through charge detectors (QD) connected to charge sensitive amplifiers. When an accelerated dust particle passes through the QD, an image charge equal and opposite to the particle's charge is induced on the detector. This measured charge and precise QD detector length allows for accurate velocity, mass, and radius calculations. Particle velocity measurements are calculated with a typical uncertainty of 0.06% (James et al., 2020). An electrostatic gate actuated by an FPGA allows for down-selection of desired particle velocities. Only dust particles with a velocity > 10 km/s were selected and allowed to enter the ablation chamber.

Thomas et al. (2017) developed a pressurized chamber to be fitted to the end of the accelerator beam line. Dust particles that enter the chamber heat and ablate, simulating a meteoroid in the upper atmosphere. Internal pressure is adjustable between 0.01 and 0.5 Torr. The chamber is fitted with four quartz windows arrayed along its length to allow for optical measurements. Additionally, an apparatus consisting of biased elec-

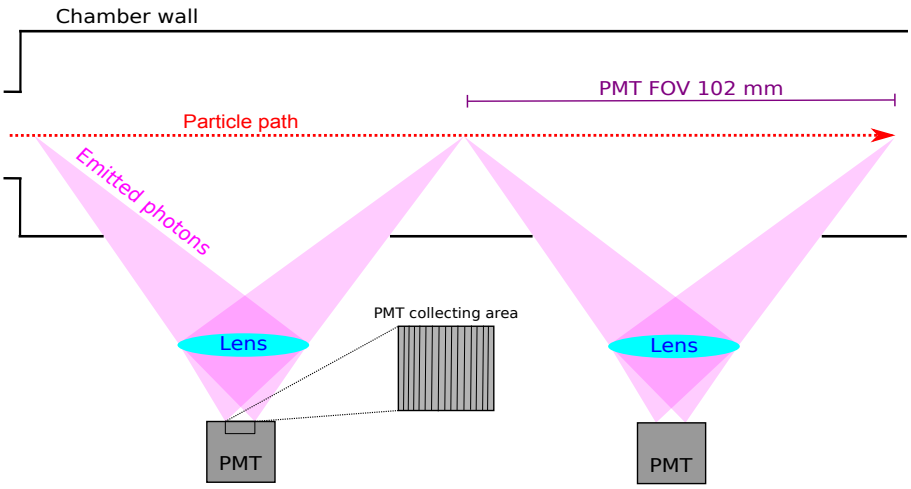

Figure 1. Schematic of the front half of the ablation chamber. Particles enter the pressurized chamber, where they begin to ablate. Photons emitted during ablation exit the chamber through one of four windows and are focused by lenses onto PMTs. The collecting area of each PMT is divided vertically into 16 pixels.

trodes placed at the top and bottom of the chamber connected to an array of charge sensitive amplifiers (CSAs) can be placed in the chamber to measure ionization during ablation. The chamber is 41 cm in length; a 20 km/s particle travels the length of the chamber in 20 μs. For this experiment, the chamber was pressurized with ambient air held at 100 mTorr.

The CSA apparatus was used to measure the ionization efficiency of iron and aluminum at meteoric speeds (Thomas et al., 2016; DeLuca et al., 2018). The ionization efficiency (β) characterizes the number of ions produced per ablated atom, on average. β is a critical parameter for determining meteor masses from radar observations (Stober et al., 2011; Tarnecki et al., 2021). DeLuca et al. (2018) also made rudimentary measurements of the light output by covering the chamber windows with slit apertures and attaching photomultiplier tubes (PMTs) to each window; however, very few photons were measured (on the order of tens of photons per event), and a conclusive measurement of the luminous efficiency was not made.

Figure 1 shows a schematic of the ablation chamber and the optical system used in this work. A 16 channel PMT (Hamamatsu H11459) is fitted to each of the four windows on the ablation chamber. A 25 mm asphere lens with a focal length of 17.5 mm is mounted between the PMT and the window; the lens collects and focuses the emitted photons, increasing the sensitivity of the system over the slit used by DeLuca et al. (2018). The collecting surface of the PMT is split in one direction into 16 0.8×16 mm channels; the PMT is positioned such that the long dimension of the pixels is perpendicular to the particle path. This arrangement provides spatial information on a channel-to-channel basis, as well as between successive PMTs. The signal output from the PMTs is sampled at 100 MHz on each channel by 14-bit AlazarTech ATS9416 digitizers.

The PMTs are sensitive to photons with wavelengths 300-920 nm. The quantum efficiency (QE) ranges from 4-20%, with peak efficiency at 600 nm. Each PMT channel is calibrated individually using a tungsten-halogen low brightness source (380-1068 nm). This process results in an empirical relationship between incident photon flux across these wavelengths and PMT response for each channel, accounting for variation in sensitiv-

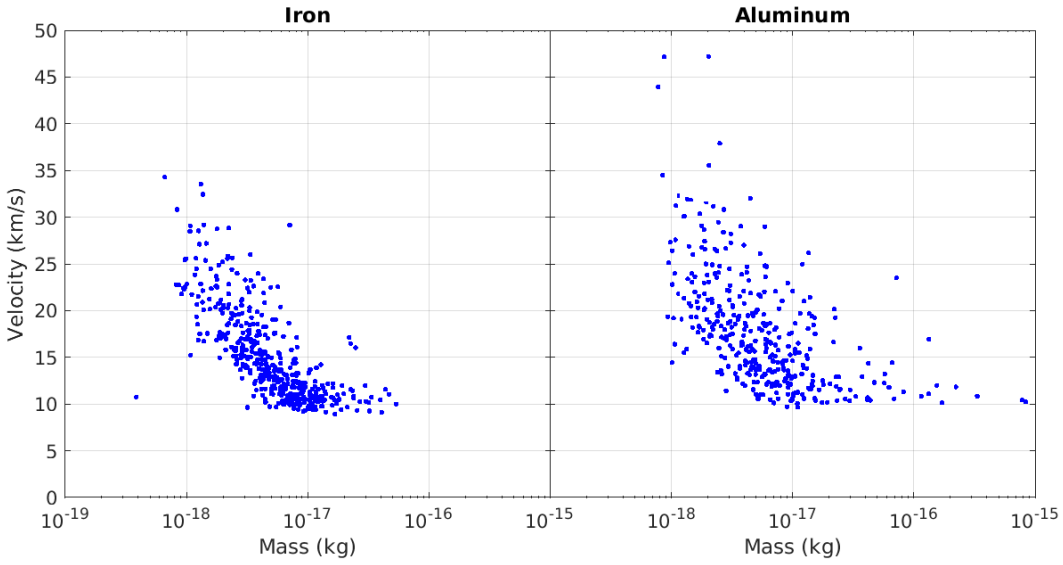

Figure 2. Particle mass as a function of velocity for iron (left) and aluminum (right) particles with detected optical signals.

ity and gain. The PMTs are operated in the linear region. The calibration relationship is applied during data processing to convert the measured voltages into photon fluxes.

3 Data and Analysis

Data were collected over 14 days (6 days with iron dust, 8 with aluminum) in June 2021 and February 2022. The ablation chamber was pressurized to 100 mTorr. A total of 17193 iron and 7570 aluminum particles were shot, of which 804 and 428 produced observable optical signals, respectively. The mass and velocity of each observed particle are shown in Figure 2. Particle mass and velocity are coupled due to the acceleration mechanism, so in general more massive particles have lower velocities. The majority of the particles have velocities of $10 - 40$ km/s and masses of $10^{-18} - 10^{-16}$ kg.

For each event, 1 ms of data is recorded with 100 MS/s resolution on each PMT channel. An example event is shown in Figure 3. Each curve shows the raw output voltage from a single channel, spaced so that channels at the entrance of the chamber are at the bottom and channels at the end are at the top. An ablating particle produces a signal 5-20 mV above the background noise level. Small spikes outside the main ablation peaks correspond to dark counts or spurious photons entering the PMTs. On a single channel, the ablation signal appears as a jagged increase in voltage 1–3 μs wide. If one were to draw a line between the centers of these increases on Figure 3, the slope of the line would be related to the particle's velocity. We find general agreement between the velocities determined by the QD system and calculated from optical signals. Bending of the curve away from a straight line indicates that the particle is decelerating.

The steps to calculate the luminous efficiency of a single particle are as follows:

1. Isolate the event, reducing the data to a 200 μs window centered on the event.
2. Subtract the background noise.
3. Use the empirical calibration relationship to convert voltages to incident photon flux.

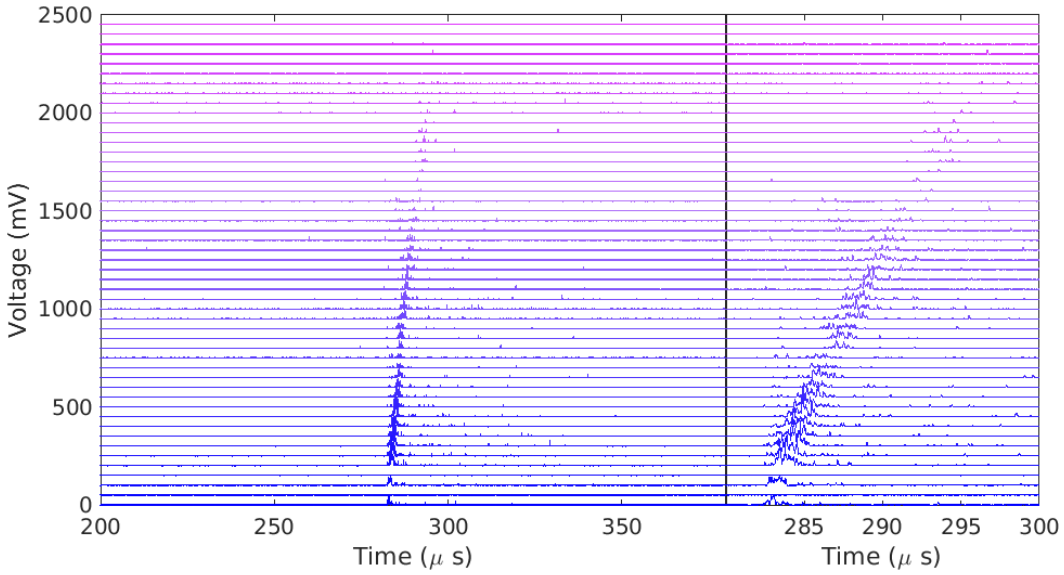

Figure 3. Example of a single ablation event; the right panel shows a zoomed in view of the event. Each horizontal line represents data from one PMT channel, with a 50 mV offset between successive channels. The data are arrayed such that channel nearest the front of the chamber is at the bottom of the plot, and the last channel is at the top. The peaks beginning at about 270 μs correspond to photons emitted during ablation; other small peaks are dark counts or spurious photons. The particle exhibits some deceleration, represented by the changing slope of the peaks.

4. Calculate the total number of emitted photons, integrating photon flux for each channel and summing channel totals.
5. Calculate the event luminosity, assuming a mean photon wavelength.
6. Calculate the luminous efficiency using Equation 1.

Mapping between the number of detected and emitted photons requires several considerations. The signal is attenuated by transmission through the lens and the quartz chamber windows. Additionally, the solid angle of the detector changes based on the point of emission. We assume the particle emits isotropically, scale by the solid angle of the detecting pixel, and account for transmission losses.

A characteristic wavelength for each species (374 nm for iron particles or 396 nm for aluminum particles) is chosen to perform the conversion between photon count and luminosity. These wavelengths correspond with the peak wavelengths in the iron and aluminum emission spectra (Nave et al., 1994; Kaufman & Martin, 1991). The luminous efficiency is directly proportional to the assumed photon energy, so any variation in the characteristic wavelength scales the luminous efficiency accordingly. It is not currently well known whether the photons emitted during ablation primarily follow the emission spectrum of the meteoroid material or the surrounding gas. Further studies are required to more correctly capture this behaviour.

In many previous studies, deceleration has been neglected by considering only the first term of Equation 1. In our analysis, we modify Equation 1 in step 6 above by integrating both sides. By considering the total kinetic energy rather than $\frac{dE_k}{dt}$, we do not neglect the change in energy due to deceleration. The consequence of applying this method is that τ is treated as a constant for a single event.

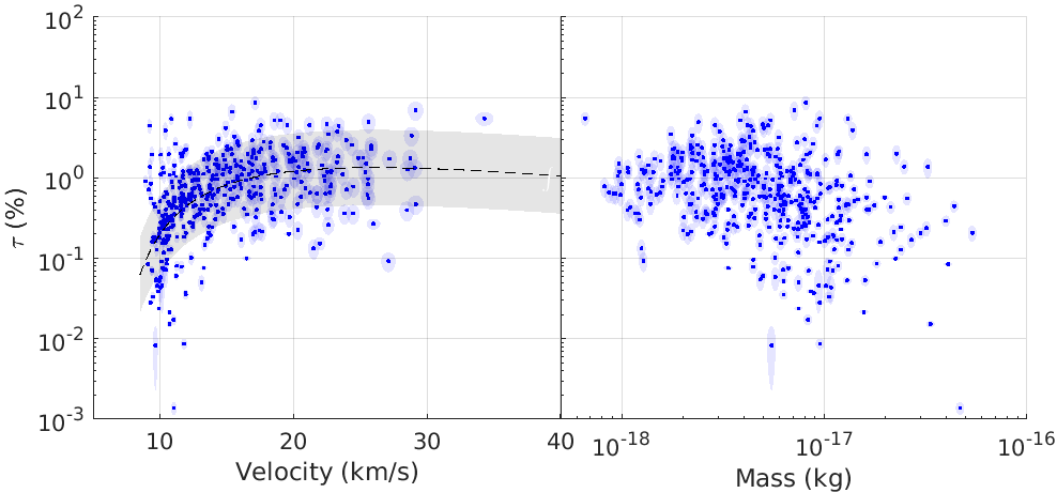

Figure 4. Luminous efficiency results for the iron campaign, plotted against velocity (left) and mass (right). Each blue point represents the luminous efficiency calculated for a single dust particle; shaded blue regions correspond to the uncertainty in velocity, mass, and luminous efficiency. The black dashed line is the best-fit to the data (Equation 2); the shaded grey region corresponds to the RMSE of 0.47.

At each step in this analysis process we propagate errors due to uncertainty in the particle mass and velocity and the voltage-photon flux calibration relationship. In this fashion, an estimate of the luminous efficiency and the associated uncertainty are calculated for each observed event. At this point, events are classified by several quality metrics; only events that completely ablate in the chamber are included in the following analysis.

4 Results

After eliminating events that did not fully ablate, 452 iron and 368 aluminum events remained. Figures 4 and 5 show the luminous efficiencies calculated for each dust particle that ablated completely in the chamber and the associated uncertainties as a function of initial particle velocity and mass, for iron and aluminum respectively. All events have velocities from 10–50 km/s.

Both sets of data share a general trend with other estimates of the luminous efficiency; as a function of velocity, the luminous efficiency is very low at velocities less than 12 or 13 km/s, then rises sharply to around 1% by about 15 km/s. However, the aluminum and the iron results differ significantly from each other in shape and magnitude, especially at higher velocities. The iron curve approximately plateaus above 15 km/s, with a slight peak around 25 km/s. In contrast, the aluminum curve peaks sharply just before 15 km/s, then turns around and decreases with increasing velocity. The two results differ by up to a factor of five in the 10-15 km/s and 25+ km/s regimes. The iron data also show significantly more spread than the aluminum data. Increased noise and detection of spurious photons during the iron collection campaign could contribute to this spread; however, the results do not significantly change when only low-noise iron events are considered in the analysis. In both cases, the 10–15 km/s velocity range shows the greatest variation, with points spread over 4 orders of magnitude in τ.

As described in Section 3, dust particle mass and velocity are coupled in this experiment. Therefore, the trends with velocity seen in the left panels of Figures 4 and 5

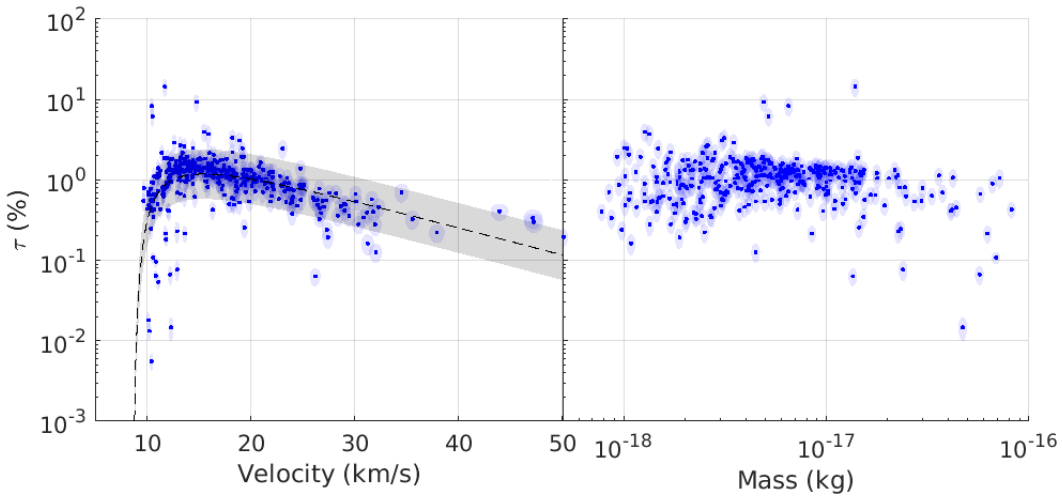

Figure 5. Luminous efficiency results for the aluminum campaign, plotted against velocity (left) and mass (right). Each blue point represents the luminous efficiency calculated for a single dust particle; shaded blue regions correspond to the uncertainty in velocity, mass, and luminous efficiency. The black dashed line is the best-fit to the data (Equation 3); the shaded grey region corresponds to the RMSE of 0.31.

are necessarily also trends with mass (e.g. particles with high velocity also have low masses). The right panels in Figures 4 and 5 show luminous efficiency plotted against mass. These results do not show any clear relationship, indicating that the trends are indeed with velocity rather than mass.

The functional form that performed best when applied to both sets of data is a rational fit with a second order polynomial in the numerator and a first order polynomial in the denominator. The best-fit to the iron data is given by Equation 2. The RMSE of the fit is 0.47 in log space; 0.5 corresponds to about a factor of 3.

$$\log \tau_{Fe} = \frac{0.019v^2 + 0.89v + 5.0}{4.1 - v} \tag{2}$$

The best-fit to the aluminum data is given by Equation 3. The RMSE of the fit is 0.31 in log space, corresponding to about a factor of 2.

$$\log \tau_{Al} = \frac{0.035v^2 + 0.84 - 7.6}{8.3 - v} \tag{3}$$

In Equations 2 and 3, v is in units of km/s; τ is in natural units, not a percentage. The fits are plotted as dashed lines in Figures 4 and 5. These fits are empirical, and do not necessarily give insight into the physics of the ablation process.

Thus far we have reported and discussed results as a function of velocity. Since velocity and mass are coupled for particles shot by the accelerator, there is also a strong trend with mass in these results. As lower mass particles are more likely to have higher velocities, they also tend to have higher luminous efficiencies. This relationship cannot be decoupled, given the constraints of this dataset.

5 Discussion and Conclusions

To put these results in the context of previous work, we consult the summary plot in Subasinghe and Campbell-Brown (2018) (Figure 9) for convenience. The iron fit (Equation 2) shares a similar form with many previous results; however, the fall-off to the left of the peak value is steeper than is typical in other works. This corresponds to a more significant "turn off" of ablation at sufficiently low speeds. Additionally, the plateau value is slightly higher than most of the examples in Subasinghe and Campbell-Brown (2018). In contrast, the aluminum fit (Equation 3) diverges significantly in form, exhibiting both a sharper rise to the peak and subsequent steeper fall off. The aluminum fit decreases by an order of magnitude from 13 km/s (the peak) to 40 km/s, behaviour that is not shared by the iron fit or any of the examples in Subasinghe and Campbell-Brown (2018).

The classical model of ablation assumes that no mass is lost until the meteoroid reaches the boiling point, at which point mass loss is proportional to v^3 (Campbell-Brown, M. D. & Koschny, D., 2004). The boiling point of aluminum is lower than that of iron by about 400°C (2862 and 2470°C, respectively). Therefore under the classical model, one would expect the aluminum particles to begin ablating closer to the front of the chamber than the iron particles. This is indeed the case in our data; in most cases, the aluminum particles show signs of ablation as soon as they enter the chamber, especially those with high velocities, while the location at which the iron particles begin ablating is more uniformly distributed over the first half of the chamber. However, at high velocities most iron events also begin ablating near the front of the chamber.

During data collection, optical signals were detected from 2–10% of particles shot by the accelerator. The low detection rate significantly increased the time required to build up a representative dataset, and raises questions regarding why some particles produced optical signals and others did not. The ablation chamber is connected to the accelerator by a small aperture, to maintain vacuum along the beam line. This aperture rejects some portion of the dust particles with trajectories from the source to the chamber aperture that are not exactly aligned. These rejections are not measureable, so we cannot attribute the low detection rate to the rejection of the majority of particles; however, this phenomenon surely plays some role.

These results imply both that a constant luminous efficiency is not sufficient over the full range of meteoric velocities, and that the luminous efficiency may not be invariable with composition in all cases. While aluminum is not typically a major component of meteoroids, the distinct difference in the luminous efficiency results between iron and aluminum sources shows that the composition of the ablating material significantly affects the resulting luminous efficiency. The results also suggest that the luminous efficiency can change by a factor of 5 or more between different species. Together, these trends showcase the need for further studies investigating additional materials and extending the range to higher velocities.

In addition to improved characterization of the luminous efficiency, the composition dependence of τ also demonstrates the need for spectroscopic data in conjunction with radar and optical meteor observations. An experiment is currently being developed to modify the apparatus used in this experiment to study ablation spectra in the laboratory, the results of which will be salient in interpreting observational spectra and give insight into the ablation process.

6 Open Research

The luminous efficiency data and particle metadata are archived at doi.org/10.5281/zenodo.7569526.

Acknowledgments

This work was supported by NSF award 1833209. The IMPACT facility is funded by SSERVI: NASA's Solar System Exploration Virtual Institute.

References

Becker, D. G., & Friichtenicht, J. F. (1971, June). Measurement and Interpretation of the Luminous Efficencies of Iron and Copper Simulated Micrometeors. *Ap. J.*, *166*, 699. doi: 10.1086/150994

Becker, D. G., & Slattery, J. C. (1973, December). Luminous Efficiency Measurements for Silicon and Aluminum Simulated Micrometeors. *Ap. J*, *186*, 1127-1140. doi: 10.1086/152576

Bland, P. A., Smith, T. B., Jull, A. J. T., Berry, F. J., Bevan, A. W. R., Cloudt, S., & Pillinger, C. T. (1996, November). The flux of meteorites to the Earth over the last 50 000 years. *Monthly Notices of the Royal Astronomical Society*, *283*(2), 551-565. doi: 10.1093/mnras/283.2.551

Brown, P., Weryk, R. J., Kohut, S., Edwards, W. N., & Krzeminski, Z. (2010, February). Development of an All-Sky Video Meteor Network in Southern Ontario, Canada The ASGARD System. *WGN, Journal of the International Meteor Organization*, *38*(1), 25-30.

Campbell-Brown, M. D., & Koschny, D. (2004). Model of the ablation of faint meteors. *A&A*, *418*(2), 751-758. doi: 10.1051/0004-6361:20041001-1

Campbell-Brown, M. D., Kero, J., Szasz, C., Pellinen-Wannberg, A., & Weryk, R. J. (2012). Photometric and ionization masses of meteors with simultaneous eiscat uhf radar and intensified video observations. *Journal of Geophysical Research: Space Physics*, *117*(A9). doi: 10.1029/2012JA017800

Ceplecha, Z. (1966, January). Dynamic and photometric mass of meteors. *Bulletin of the Astronomical Institutes of Czechoslovakia*, *17*, 347.

Ceplecha, Z., Borovička, J., Elford, W. G., Revelle, D. O., Hawkes, R. L., Porubčan, V., & Šimek, M. (1998, September). Meteor Phenomena and Bodies. *Space Science Reviews*, *84*, 327-471. doi: 10.1023/A:1005069928850

DeLuca, M., Munsat, T., Thomas, E., & Sternovsky, Z. (2018). The ionization efficiency of aluminum and iron at meteoric velocities. *Planetary and Space Science*, *156*, 111-116. doi: 10.1016/j.pss.2017.11.003

Dyrud, L. P., Denney, K., Urbina, J., Janches, D., Kudeki, E., & Franke, S. (2004). The meteor flux: it depends how you look. *Earth, Moon, and Planets*, *95*(1), 89–100. doi: 10.1007/s11038-005-9001-6

James, D., Fontanese, J., Munsat, T., & Horányi, M. (2020). Calibration methods of charge sensitive amplifiers at the colorado dust accelerator. *Review of Scientific Instruments*, *91*(11), 113301. doi: 10.1063/5.0020018

Kaufman, V., & Martin, W. C. (1991). Wavelengths and energy level classifications for the spectra of aluminum (ali through alxiii). *Journal of Physical and Chemical Reference Data*, *20*(5), 775-858. doi: 10.1063/1.555895

Mathews, J. D., Janches, D., Meisel, D. D., & Zhou, Q. H. (2001). The micrometeoroid mass flux into the upper atmosphere: Arecibo results and a comparison with prior estimates. *Geophysical Research Letters*, *28*(10), 1929-1932. doi: 10.1029/2000GL012621

Nave, G., Johansson, S., Learner, R. C. M., Thorne, A. P., & Brault, J. W. (1994, September). A New Multiplet Table for Fe i. *Astrophysical Journal Supplement*, *94*, 221. doi: 10.1086/192079

Plane, J. M. C. (2012). Cosmic dust in the earth's atmosphere. *Chem. Soc. Rev.*, *41*, 6507-6518. doi: 10.1039/C2CS35132C

Shu, A., Collette, A., Drake, K., Grün, E., Horányi, M., Kempf, S., ... Thomas, E. (2012). 3 mv hypervelocity dust accelerator at the colorado center for lunar

dust and atmospheric studies. *Review of Scientific Instruments*, *83*(7), 075108. doi: 10.1063/1.4732820

Spurný, P., & Borovička, J. (2002, November). The autonomous all-sky photographic camera for meteor observation. In B. Warmbein (Ed.), *Asteroids, comets, and meteors: Acm 2002* (Vol. 500, p. 257-259).

Stober, G., Jacobi, C., & Singer, W. (2011). Meteoroid mass determination from underdense trails. *Journal of Atmospheric and Solar-Terrestrial Physics*, *73*(9), 895-900. doi: 10.1016/j.jastp.2010.06.009

Subasinghe, D., & Campbell-Brown, M. (2018, February). Luminous Efficiency Estimates of Meteors. II. Application to Canadian Automated Meteor Observatory Meteor Events. *Astronomical Journal*, *155*(2), 88. doi: 10.3847/1538-3881/aaa3e0

Tarnecki, L. K., Marshall, R. A., Stober, G., & Kero, J. (2021). Meteoroid mass estimation based on single-frequency radar cross section measurements. *Journal of Geophysical Research: Space Physics*, *126*(9), e2021JA029525. (e2021JA029525 2021JA029525) doi: 10.1029/2021JA029525

Thomas, E., Horányi, M., Janches, D., Munsat, T., Simolka, J., & Sternovsky, Z. (2016). Measurements of the ionization coefficient of simulated iron micrometeoroids. *Geophysical Research Letters*, *43*(8), 3645-3652. doi: 10.1002/2016GL068854

Thomas, E., Simolka, J., DeLuca, M., Horányi, M., Janches, D., Marshall, R. A., ... Sternovsky, Z. (2017). Experimental setup for the laboratory investigation of micrometeoroid ablation using a dust accelerator. *Review of Scientific Instruments*, *88*(3), 034501. doi: 10.1063/1.4977832

Vida, D., Šegon, D., Gural, P. S., Brown, P. G., McIntyre, M. J. M., Dijkema, T. J., ... Zubović, D. (2021, August). The Global Meteor Network – Methodology and first results. *Monthly Notices of the Royal Astronomical Society*, *506*(4), 5046-5074. doi: 10.1093/mnras/stab2008

Figure 1.

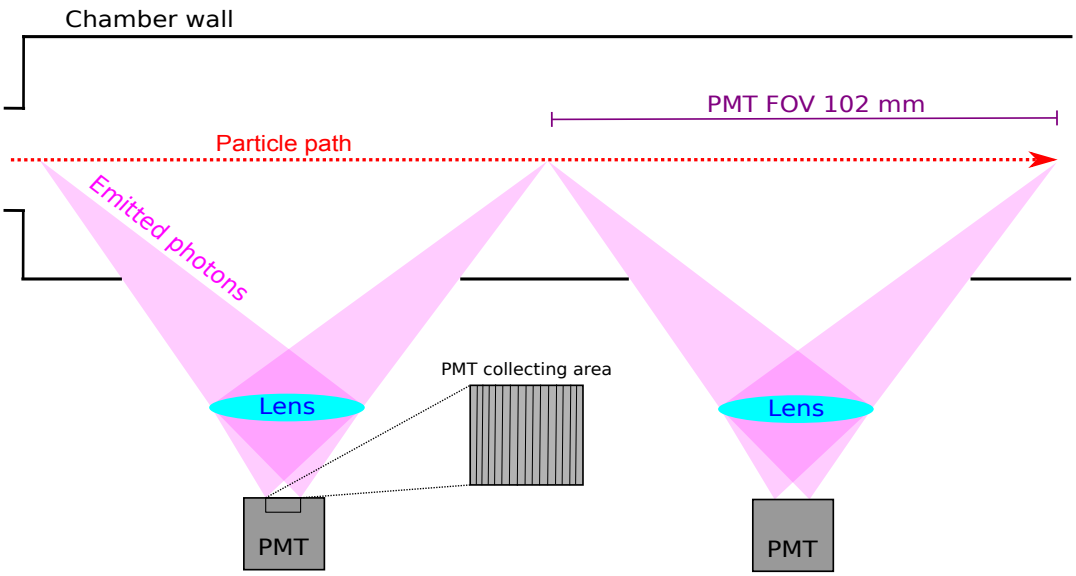
Chamber wall
PMT FOV 102 mm
Particle path
Emitted photons
PMT collecting area
Lens
Lens
PMT
PMT

Figure 2.

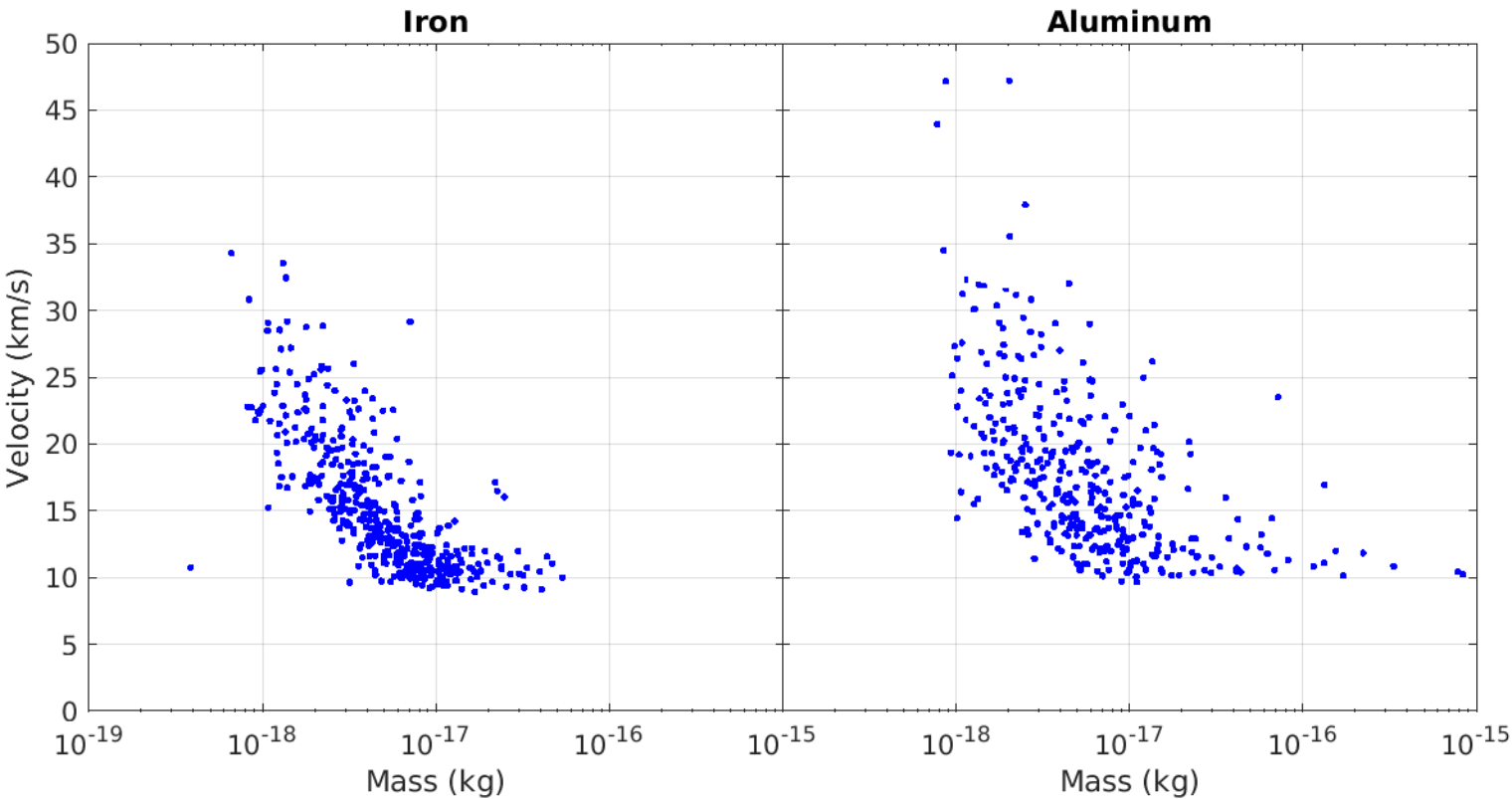
Iron
Aluminum
Velocity (km/s)
Mass (kg)
Mass (kg)
0
5
10
15
20
25
30
35
40
45
50
10^-19
10^-18
10^-17
10^-16
10^-15
10^-18
10^-17
10^-16
10^-15

Figure 3.

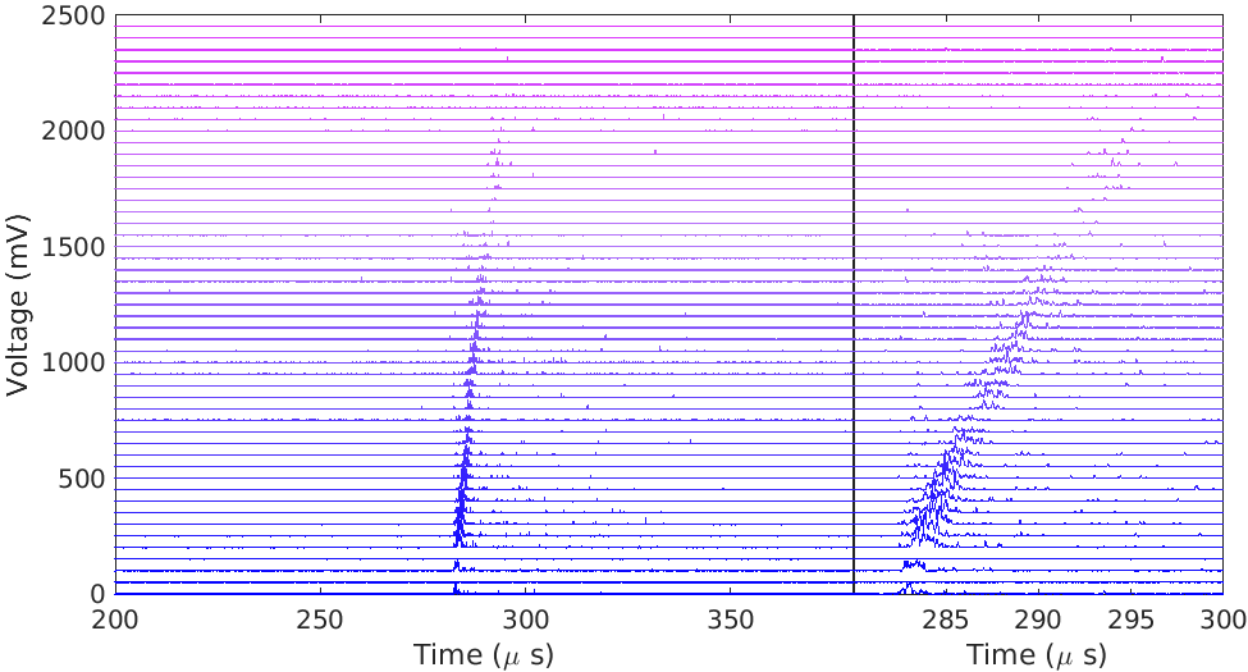
2500
2000
1500
1000
500
0
Voltage (mV)
200
250
300
350
Time (μ s)
285
290
295
300
Time (μ s)

Figure 4.

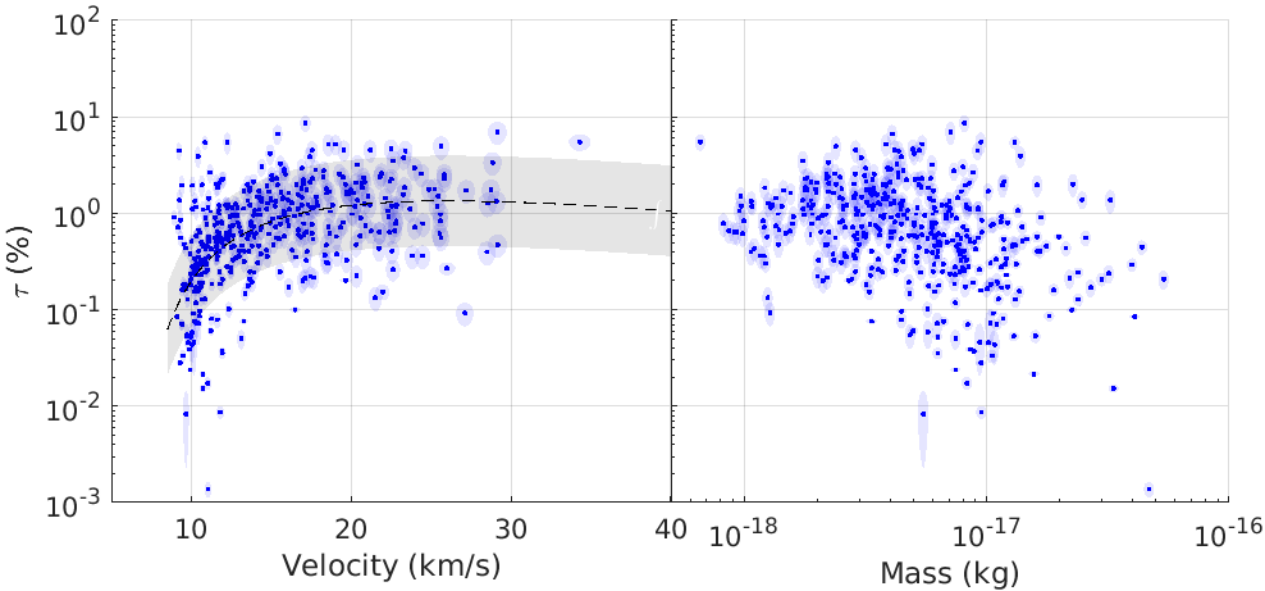
10^2
10^1
10^0
10^{-1}
10^{-2}
10^{-3}
τ (%)
10
20
30
40
Velocity (km/s)
10^{-18}
10^{-17}
10^{-16}
Mass (kg)

Figure 5.

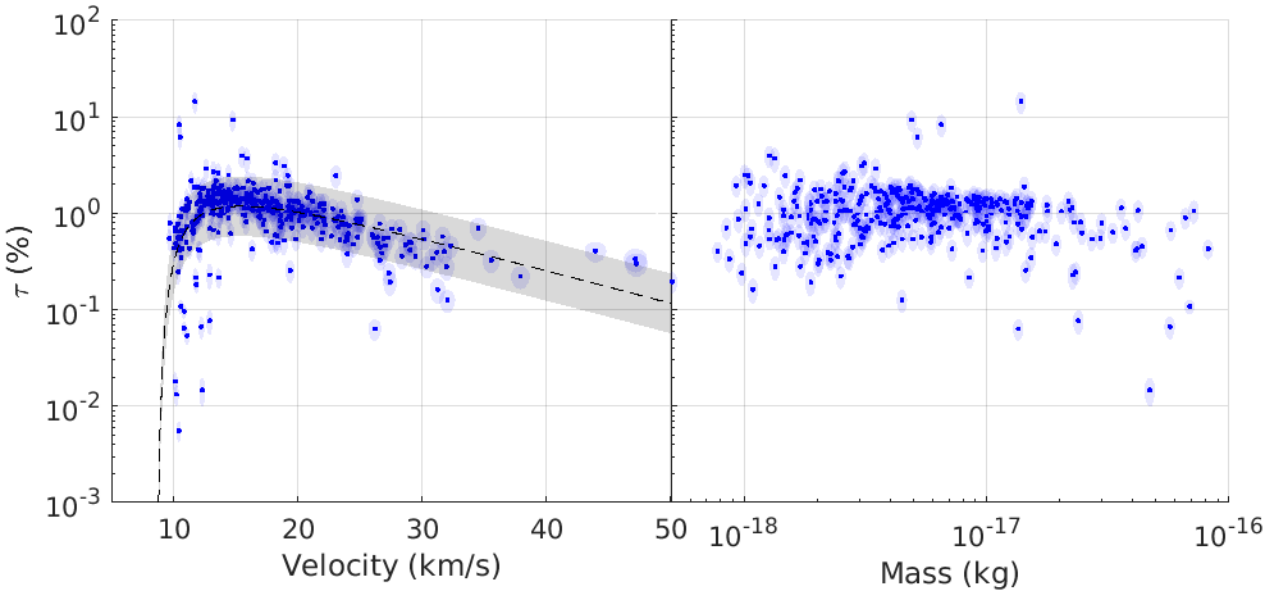
10^2
10^1
10^0
10^{-1}
10^{-2}
10^{-3}
τ (%)
10
20
30
40
50
Velocity (km/s)
10^{-18}
10^{-17}
10^{-16}
Mass (kg)